

Hydrodynamics of Immiscible Binary Fluids with Viscosity Contrast: A multiparticle collision dynamics approach

Zihan Tan,^{1,*} Vania Calandrini,² Jan K. G. Dhont,^{1,3} Gerhard Nägele,^{1,3} and Roland G. Winkler⁴

¹*Biomacromolecular Systems and Processes, Institute of Biological Information Processing,
Forschungszentrum Jülich, 52428 Jülich, Germany*

²*Computational Biomedicine, Institute for Advanced Simulation,
Forschungszentrum Jülich, 52428 Jülich, Germany*

³*Heinrich-Heine Universität Düsseldorf, Department of Physics, D-40225 Düsseldorf, Germany*

⁴*Theoretical Physics of Living Matter, Institute for Advanced Simulation,
Forschungszentrum Jülich, 52428 Jülich, Germany*

A multiparticle collision dynamics (MPC) implementation of layered immiscible fluids A and B of different shear viscosities separated by planar interfaces is presented. The simulated flow profiles for imposed steady shear motion and the mean shear stress functions are in excellent agreement with continuum hydrodynamics predictions. The wave-vector dependent transverse velocity auto-correlation functions (TVAF) in the bulk-fluid regions of the layers decay exponentially, and agree with those of single-phase isotropic MPC fluids. In addition, the hydrodynamic mobilities of an embedded colloidal sphere moving steadily parallel or transverse to a fluid-fluid interface are determined as function of the distance from the interface. The obtained mobilities are in good agreement with hydrodynamic force multipoles calculations, for a no-slip sphere moving under creeping flow conditions near a clean, ideally flat interface. The proposed MPC fluid-layer model can be straightforwardly implemented and it is computationally very efficient. Yet, owing to the spatial discretization inherent to the MPC method, the model can not reproduce all hydrodynamic features of an ideally flat interface between immiscible fluids.

I. INTRODUCTION

Multi-phase fluid flows occur ubiquitously in nature and engineering processes. Examples constitute oil-water flows, fluids with air bubbles, emulsions, dairy products, biological fluids, processing of paints, coating, and printing. Owing to their complexity, the theoretical description and efficient modeling of binary fluids pose major challenges, which stimulated a wealth of endeavors to model binary fluids using mesoscale simulations. In the lattice-Boltzmann method (LBM), the implementation of multi-phase flows and phase separation encompasses several variants: the color gradient model [1–3], the pseudo-potential model [4, 5], the free-energy functional model [6, 7], and the mean-field model [8], or combinations thereof [9]. Dissipative particle dynamics (DPD) simulations, which explicitly account of conservative pair interactions between fluid particles, allow to realize multi-phase fluids via assigning distinct interactions between the particles [10]. Furthermore, the multiparticle collision dynamics (MPC) method, a particle-based hydrodynamic simulation approach which captures hydrodynamic interactions and thermal fluctuations [11–17], has been proven valuable and efficient for mesoscale simulations, and has been applied in a broad range of studies of biological and active polymers [18–26], colloids [27–31], proteins [32, 33], vesicles and blood cells [34, 35], microswimmers [36–46], and microfluidics [47, 48]. To date, various MPC implementations of binary fluid mixtures have been proposed, and their phase behavior has

been studied [49–56]. Depending on the applied interaction rule between the different fluid components, the viscosity values of the (two) fluids are equal or individually controlled [52, 55].

Most of the above mentioned simulation methods are aimed to account for both the hydrodynamics and thermodynamics. The large computational costs, which are often necessary to suitably account for the thermodynamics involved in studying phase separation of multi-phase fluids, are dispensable when the dynamics of embedded objects such as proteins, polymers, or living organisms are considered. In fact, a plethora of physical phenomena related to immiscible binary fluids take place under conditions where phase separation is absent or is of no interest, and simulation methods accounting for the hydrodynamics alone suffice here. The MPC approach is very well suited to efficiently simulate hydrodynamic flow properties in the presence of thermal fluctuations (fluctuating hydrodynamics) [14]. In particular, MPC allows to tune the viscosity of fluids through the specification of the frequency of MPC collisions, and, hence, to control the viscous properties of immiscible fluids.

In this work, we present a model for planar layers of two immiscible binary fluids A and B using the MPC approach. The fluids, separated by a flat interface, are of distinct shear viscosity, η_A and η_B , whose values are tuned by the corresponding MPC collision frequency. While omitting the thermodynamic and kinetic processes of phase separation, it allows for fluid particle exchange across the interface, associated with an $A \leftrightarrow B$ identity switch of the MPC particles in the arriving single-fluid layer. No explicit interactions between fluid particles at the interfacial zone are required, although a more sophis-

* z.tan@fz-juelich.de

ticated modeling of the interface properties is possible for future assessment. Shear flow profiles and transverse hydrodynamic velocity correlation functions (TVAFs) are determined for the different layers. Moreover, the hydrodynamic mobility/friction properties of a colloidal sphere inside a fluid layer, which moves steadily parallel or perpendicular to an interface, are calculated. The model recovers the correct flow profiles, fluctuating hydrodynamic properties, and thermal fluctuations of the individual fluid layers. The invoked simplifications in the present MPC treatment lead to a higher computational efficiency compared to other mesoscale techniques and MPC implementations considered so far [51–56], which is a significant advantage when simulating large-scale systems.

The present simulations constitute a first important step in studying the dynamics, e.g., of monolayers of thermal particles moving near a planar fluid-fluid interface, with full account of the time-resolved (retarded) hydrodynamic interactions of the particles with the interface and among each other. These so-called quasi-two-dimensional systems have been intensely studied recently, since they reveal peculiar dynamic features such as the anomalous hydrodynamic enhancement of lateral collective diffusion [57–60], and the influence of the interface on the motion of nearby Brownian particle, as reflected in the non-isotropic, hydrodynamic long-time tails of particle velocity correlations [61, 62]. Interestingly enough, the motion pattern of microswimmers is also strongly affected by their hydrodynamic interaction with a nearby (fluid) interface [63, 64].

Our two-fluids MPC model is also a first step toward mesoscopic simulations of the diffusion and phase behavior of assemblies of interacting proteins attached to or embedded inside a membrane. It should be recognized here that the biophysical properties of the membrane, both in physiological and in vitro conditions, influence the structure and function of many membrane-associated proteins [65–71]. Diffusion properties of single membrane receptor proteins and their orientation-dependent interaction potentials (which can be partially due to local membrane deformations) as obtained from force-field based molecular dynamics (MD) simulations where the lipids and the atomistic structure of the receptor are explicitly accounted for, can be used as input to tune mesoscopic MPC simulations.

The present paper is organized as follows. Section II gives the essentials of the single-phase MPC algorithm, outlines its extension to immiscible multi-phase fluids, describes the coupling rules of a colloid with the MPC fluid, and defines the simulation parameters. The two-fluids MPC model is validated in the three subsequent sections. In section III, the shear profile of a planar three-layers system, and the corresponding time-dependent mean shear stress, are simulated and compared with continuum hydrodynamics and analytical theories. In section IV, MPC simulated transverse velocity correlation functions (TVCFs) in the bulk regions of the two

fluids, and in a region including the interface between them, are contrasted with predictions from the linearized fluctuating Landau-Lifshitz Navier-Stokes equation. In Section V, the simulated hydrodynamic mobilities of a colloidal sphere moving steadily inside the middle layer of a three-layers fluid system are compared to previous numerical results based on the Stokes equation of low-Reynolds number hydrodynamics. Finally, in section VI we summarize and conclude our findings, and provide a perspective on future work.

II. MODEL

A. Multiparticle collision dynamics (MPC) fluid

A single-phase MPC fluid consists of N point particles each of mass m , typically enclosed in a cubic simulation box of length L with periodic boundary conditions. The dynamics of the fluid particles proceeds through discrete streaming and collision steps [11–13, 72]. During a streaming step, the particles move ballistically for a time span h , referred to as collision time. Hence, the position \mathbf{r}_i of a fluid particle i , with $i \in \{1, \dots, N\}$, is updated according to

$$\mathbf{r}_i(t+h) = \mathbf{r}_i(t) + h\mathbf{v}_i(t), \quad (1)$$

where \mathbf{v}_i is the particle velocity. In the subsequent collision step, accounting for the interactions between fluid particles, the MPC particles are sorted into cubic cells of size a defining the local interaction environment (collision cells). In the stochastic rotational dynamics (SRD) variant of MPC, MPC-SRD, the relative particle velocities $\tilde{\mathbf{v}}_i = \mathbf{v}_i - \mathbf{v}_{cm}$, with respect to the center-of-mass velocity \mathbf{v}_{cm} of a particular collision cell, are rotated around a randomly orientated axis by a fixed angle α [12, 13, 73]. In three dimensions, the velocity of a particle i after a collision is thus given by

$$\begin{aligned} \mathbf{v}_i(t+h) = & \mathbf{v}_{cm}(t) + \tilde{\mathbf{v}}_{i,\perp}(t) \cos(\alpha) \\ & + [\tilde{\mathbf{v}}_{i,\perp}(t) \times \mathfrak{R}] \sin(\alpha) + \tilde{\mathbf{v}}_{i,\parallel}(t), \end{aligned} \quad (2)$$

where \mathfrak{R} is a unit vector along the selected rotation axis, and $\tilde{\mathbf{v}}_{i,\perp}$ and $\tilde{\mathbf{v}}_{i,\parallel}(t)$ are the parallel and perpendicular components of the velocity $\tilde{\mathbf{v}}_i$ with respect to the vector \mathfrak{R} , respectively. The orientation of \mathfrak{R} is chosen independently for each collision cell and time step. The MPC-SRD algorithm conserves particle number, energy, and linear momentum. However, the employed discretization into collision cells breaks Galilean invariance, which is re-established by a random shift of the collision cell lattice at every collision step [74]. To maintain a constant temperature, a (simple) cell-level scaling scheme of the relative velocities $\tilde{\mathbf{v}}_i$ is employed [75]. Since mass, momentum and energy are conserved locally, the correct fluctuating hydrodynamic equations for an isothermal compressible fluid are captured in the continuum limit.

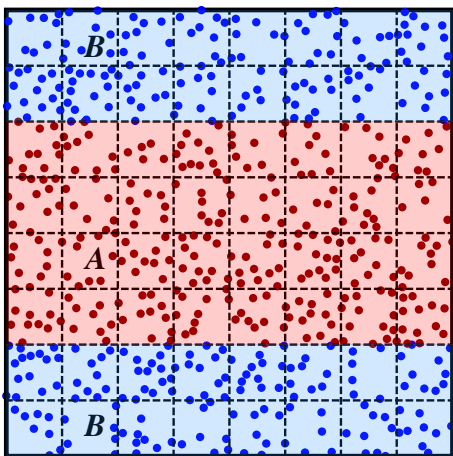


FIG. 1: Schematics of a periodic three-layer MPC system of two immiscible fluids A (red) and B (blue) separated by planar interfaces. MPC collisions are performed independently in cubic collision cells, delineated by the dashed lines, using collision times h_A and h_B according to the fluid type.

B. Immiscible binary fluid system

The extension from a single to a layered two-fluid system of phases A and B with distinct shear viscosities η_A and η_B , which are separated by two flat interfaces, is rather straightforward and illustrated in Fig. 1. As the viscosity of a single-phase MPC fluid is sensitive to the collision time h [12, 76], fluid layers A and B of different viscosities are described by using accordingly different collision time steps h_A and h_B . Without loss of generality, we take $h_A < h_B$ in the following, implying the viscosity of fluid A to be larger than that of fluid B . Furthermore, A and B particles are assumed to be of equal mass m , and the mean mass densities of both fluid phases are taken to be the same.

As for a single-phase fluid, the fluid particles move ballistically and undergo independent collisions. However, in order to prevent a density discontinuity in the vicinity of a planar interface due to discretization of time, the smaller collision time, h_A , is used in the streaming step for all fluid particles. Hence in fluid B , h_B/h_A ballistic time steps are executed before the collision step. This does not affect the properties of the bulk part of fluid B , since the particles are moving ballistically. However, it affects the B particles close to the planar A - B interface due to the random shift of the collision lattice normal to the interface. Fluid- B particles at distances $\lesssim a$ to the (mean) interface experience more collisions than in the bulk region. As a consequence, the interface is not sharp but broadened at least over the size a of a collision cell.

C. Colloid dynamics and fluid coupling

The translational and rotational motions of a neutrally buoyant no-slip hard-sphere colloid of radius R and mass M embedded in the MPC fluid is governed by elastic collisions with the MPC particles, which we account for in a coarse-grained manner [17]. During the streaming step, just as for the solvent particles, a colloidal sphere moves ballistically with center-of-mass velocity $\mathbf{V}_c(t)$. Its center-of-mass position vector, $\mathbf{R}_c(t)$, changes according to

$$\mathbf{R}_c(t+h) = \mathbf{R}_c(t) + h\mathbf{V}_c(t). \quad (4)$$

MPC particles i which (virtually) penetrate the colloid are moved backwards in time by the time interval $(h - h_i)$, where $h_i < h$ follows from the condition $|\mathbf{r}_i(t) - \mathbf{R}_c(t) + h_i(\mathbf{v}_i(t) - \mathbf{V}_c(t))|^2 = R^2$. These MPC particles collide then with a virtual colloid at the center position $\mathbf{R}_c(t) + h_i\mathbf{V}_c(t)$, transfer the momentum \mathbf{p}_i elastically to the colloid, and subsequently move with new velocity $\mathbf{v}'_i = \mathbf{v}_i(t+h_i)$ for the time interval $(h - h_i)$. The linear and angular velocities of the MPC particles and of the colloid before and after collision are related by

$$\mathbf{v}'_i = \mathbf{v}_i(t) - \mathbf{p}_i/m, \quad (5)$$

$$\mathbf{V}_c(t+h) = \mathbf{V}_c(t) + \sum_{i=1} \mathbf{p}_i/M, \quad (6)$$

$$\mathbf{\Omega}_c(t+h) = \mathbf{\Omega}_c(t) + R \sum_{i=1} (\mathbf{n}_i \times \mathbf{p}_i)/I. \quad (7)$$

The sum extends over all fluid particles colliding with the colloid during the time interval h . Here, $\mathbf{\Omega}_c$ is the angular velocity of the embedded colloid, $\mathbf{n}_i = (\mathbf{r}_i - \mathbf{R}_c)/|\mathbf{r}_i - \mathbf{R}_c|$ is the unit vector pointing from the colloid center to the position of fluid particle i , and $I = \chi MR^2$ with $\chi = 2/5$ is the moment of inertia of the spherical colloid.

To realize the hydrodynamic no-slip boundary conditions at the colloid surface, we use the bounce-back rule for the MPC fluid particles, which yields [17, 77–80]

$$\mathbf{p}_i = 2\mu\check{\mathbf{v}}_{i,n} + 2\mu\frac{M\chi}{\mu + M\chi}\check{\mathbf{v}}_{i,t}, \quad (8)$$

with the relative velocity, $\check{\mathbf{v}}_i$, of a colliding MPC fluid particle i with respect to the according colloid surface point given by

$$\check{\mathbf{v}}_i = \mathbf{v}_i - [\mathbf{V}_c + R\mathbf{\Omega}_c \times \mathbf{n}_i]. \quad (9)$$

Here, $\mu = mM/(m+M)$ is the reduced mass, and $\check{\mathbf{v}}_{i,n}$ and $\check{\mathbf{v}}_{i,t}$ are the normal and tangential relative velocity parts, respectively, with respect to the colloid surface.

In the MPC collision step, phantom (p) solvent particles are added inside the colloid to enforce the no-slip hydrodynamic boundary condition [81]. These particles are uniformly distributed inside the colloid according to

the average MPC-fluid particle density, and their velocities relative to the colloidal translational and rotational velocities are taken from a central Maxwellian distribution function. This yields the updated colloid translational and angular velocities after a collision step

$$\mathbf{V}_c(t+h) \rightarrow \mathbf{V}_c(t+h) + \sum_i \Delta \mathbf{p}_i^p / M, \quad (10)$$

$$\mathbf{\Omega}_c(t+h) \rightarrow \mathbf{\Omega}_c(t+h) + R \sum_i (\mathbf{r}_i^p - \mathbf{R}_c) \times \Delta \mathbf{p}_i^p / I, \quad (11)$$

respectively. Here, $\Delta \mathbf{p}_i^p$ denotes the change in the linear momentum of phantom particle i at position \mathbf{r}_i^p due to SRD, and $\mathbf{V}_c(t+h)$ and $\mathbf{\Omega}_c(t+h)$ are the velocities in Eqs. (6) and (7), respectively.

To further speed up the simulations, we use a common value $h_i = h/2$ for all MPC particles rather than considering the individual elastic collision events at the exact times $t+h_i$ of each fluid particle-colloid collision. This simplifying step was shown to be as accurate as when the exact h_i s are used, especially for small collision time steps [77, 79, 82].

D. Simulation parameters

In what follows, lengths are measured in units of a , mass in units of m , and energy in units of the thermal energy $k_B T$. We use therefore the units

$$t_0 = \sqrt{ma^2/(k_B T)} \quad (12)$$

$$\nu_0 = a^2/t_0 = a\sqrt{k_B T/m} \quad (13)$$

$$\eta_0 = m/(at_0) = \sqrt{mk_B T}/a^2 \quad (14)$$

for time, t_0 , kinematic viscosity, ν_0 , and viscosity, η_0 , respectively. Note that t_0 is equal to the ratio of cell size a and thermal velocity $v_{th} = \sqrt{k_B T/m}$. The average number of particles per collision cell is selected as $\langle N_c \rangle = 10$, implying equal mean number and mass densities of the A and B fluids, and the rotation angle is set to $\alpha = 130^\circ$. The collision time steps are taken as $h_A = h_B/5 = 0.02 \times t_0$. These parameters determine the fluid transport properties in the bulk region, e.g., the shear viscosities are $\eta_A = 41.2 \eta_0$ and $\eta_B = 8.7 \eta_0$ [72, 73, 75, 76, 83, 84], giving the viscosity ratio $\eta_B/\eta_A \approx 0.21$. With the mass density $\rho = \langle N_c \rangle m/a^3$, the corresponding kinematic viscosities are $\nu_A/\nu_0 = 4.12$ and $\nu_B/\nu_0 = 0.87$. The related dimensionless Schmidt numbers are $Sc_A = \nu_A/D_A = 400$ and $Sc_B = \nu_B/D_B = 17$, expressing that the viscous diffusion of (transversal) momentum in the fluid is distinctly faster than diffusive mass transport, with the latter characterized by the mass diffusion coefficients $D_A = (h_A/h_B)D_B \propto D_0$ of fluid A and B particles, respectively, where $D_0 = a^2/t_0$ is the unit of mass diffusion. Simulations are performed using periodic boundary conditions, applied in sections III and

IV to a cubic simulation box of length $L/a = 39$ and 80, respectively, and in section V to a rectangular box of lengths $2L_x/a = 2L_y/a = L_z/a = 80$. The latter embeds a colloidal sphere of radius $R = 2.5a$.

III. SHEAR SIMULATIONS

As a first example used for scrutinizing the hydrodynamic behavior of our two-fluids MPC approach, we consider a standard stationary shear flow setup as sketched in Fig. 2. The three planar layers of two immiscible fluids A and B are sheared by two walls oriented parallel to the xy -plane, which moving oppositely along the x -direction with velocities $\pm u = 0.0975 v_{th}$. The lower wall is located at $z = 0$ and the upper one at $z = L_z = L = 39a$. No-slip boundary conditions (BCs) at the walls are implemented using the bounce-back rule and phantom particles inside the walls [76]. The three symmetric B - A - B fluid layers are separated by planar interfaces located at $z = L_z/4$ and $3L_z/4$, respectively.

The according laminar shear velocity $\mathbf{v} = v_x(z) \mathbf{e}_x$, as obtained from the Navier-Stokes equation [85], is piecewise linear and unidirectional in x -direction along the unit vector \mathbf{e}_x and hence incompressible. The flow is uniquely determined by the wall-fluid stick boundary conditions, and the continuity of flow velocity and shear stress across the two clean planar interfaces whose thickness is assumed to be zero. Explicitly,

$$v_x^B(L_z) = -v_x^B(0) = u, \quad (15)$$

$$v_x^A(L_z/4) = v_x^B(L_z/4) = u_s^-, \quad (16)$$

$$v_x^A(3L_z/4) = v_x^B(3L_z/4) = u_s^+, \quad (17)$$

where u_s^+ and $u_s^- = -u_s^+$ (by symmetry) are the velocities of the upper and lower fluid interface, respectively. The interfacial velocities are obtained using the continuity of shear stress across the planar clean interfaces (no Marangoni stress and Laplace pressure)

$$\eta_A \dot{\gamma}_A = \eta_B \dot{\gamma}_B, \quad (18)$$

at $z = L_z/4$ and $3L_z/4$, respectively, which yields

$$u_s^\pm = \pm \frac{\eta_B}{\eta_B + \eta_A} u. \quad (19)$$

Here, $\dot{\gamma}_A = du_x^A(z)/dz$ and $\dot{\gamma}_B = du_x^B(z)/dz$ are the constant shear rates in the two layers of fluid A , and the mid-layer of fluid B , respectively. The (dynamic) pressure for the unidirectional shear flow is constant throughout the system including the interfaces.

The MPC simulation results for $v_x(z)$ displayed in Fig. 3(a) reflect the hydrodynamically expected behavior of three linear shear flow regions. Even more, the simulation results agree quantitatively with the hydrodynamic flow profile described in Eqs. (15) - (19). In spite of the non-zero thickness of the interface in the MPC simulations of the order of the collision cell size a , caused by

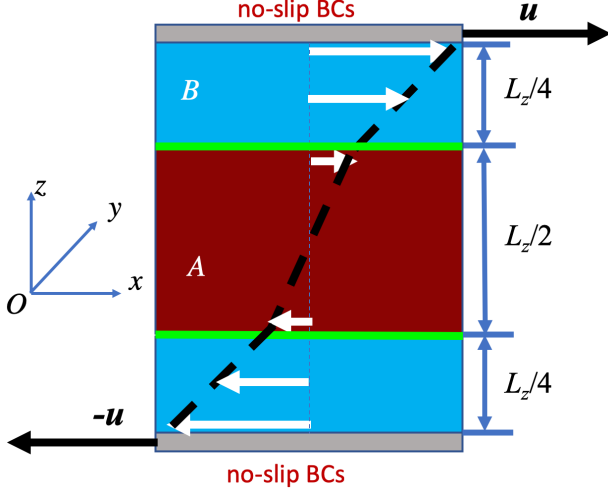


FIG. 2: Schematics of a layered B - A - B fluid system steadily sheared by two parallel no-slip walls moving in opposite direction with the velocities $\pm \mathbf{u} = (\pm u, 0, 0)$. A piece-wise linear velocity profile is obtained from hydrodynamics under stationary laminar flow conditions.

discretization in terms of collision cells and random shift of the collision cell lattice, the MPC results suggest that the interface width is of minor relevance for fluid properties on lengths scales significantly larger than a . The inset of Fig. 3(a) magnifies the velocity profile in the A - B interfacial region. It suggests a continuous change both of $v_x(z)$ and its slope across the interface. This indicates also a continuous change of the *local* viscosity in the interfacial region caused by the discretization.

The mean shear stress in the considered shear-flow setup should be spatially constant throughout the system volume $V = L^3$ between the upper and lower walls. To confirm its constancy under steady-state conditions, and to show that the hydrodynamically expected relations between stress, shear rate, and viscosity are recovered in the MPC simulations, we calculate the average shear stress based on its internal (superscript i) as well as external (superscript e) expressions. Explicitly, the instantaneous values of the external, σ_{xz}^e , and internal, σ_{xz}^i , shear stresses are [76]

$$\begin{aligned} \sigma_{xz}^e &= \frac{L}{2Vh_B} \left(\sum_{i=1}^N \Delta p_{ix}^u - \sum_{i=1}^N \Delta p_{ix}^l \right) \\ &+ \frac{L}{2Vh_B} \left(\sum_{i \in bc} \Delta p_{ix}^u - \sum_{i \in bc} \Delta p_{ix}^l \right), \end{aligned} \quad (20)$$

$$\begin{aligned} \sigma_{xz}^i &= -\frac{1}{V} \sum_{i=1}^N m \hat{v}_{ix} \hat{v}_{iz} + \frac{2u}{Vh_B} \sum_{i=1}^N m \hat{v}_{iz} \Delta t_q^i \\ &- \frac{1}{Vh_{A(B)}} \sum_{i=1}^N \Delta p_{ix} r_{iz} + \frac{L}{2Vh_B} \left(\sum_{i \in bc} \Delta p_{ix}^u - \sum_{i \in bc} \Delta p_{ix}^l \right), \end{aligned} \quad (21)$$

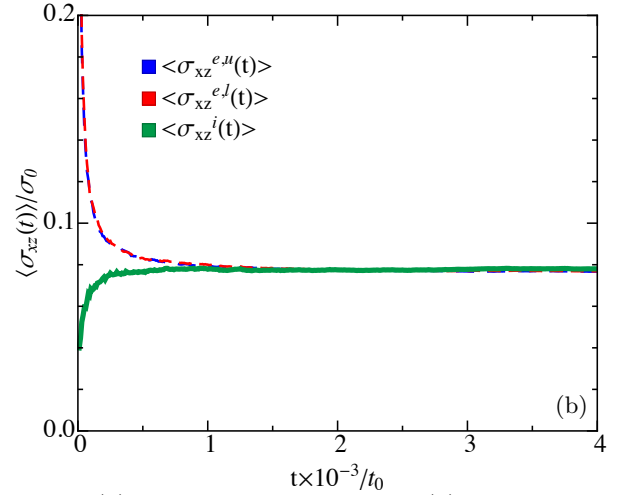
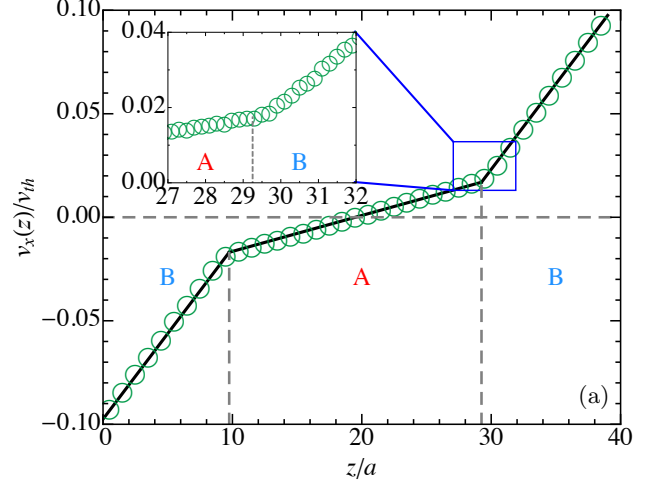


FIG. 3: (a) Shear velocity profile, $v_x(z)$, of a B - A - B fluid layer system obtained from MPC simulations (circles) and analytically from continuum hydrodynamics (lines) according to Eqs. (15) - (19). The magnitude of the wall velocity is $|u| = 0.0975v_{th}$. Inset: Magnification of $v_x(z)$ in the A - B interfacial region (blue rectangle). (b) Magnitude of the time-dependent mean external shear stress, $\langle \sigma_{xz}^{e,u/l} \rangle$, calculated at the upper (superscript: u) and lower (superscript: l) wall, as well as the internal shear stress $\langle \sigma_{xz}^i \rangle$ in units of thermal stress $\sigma_0 = k_B T / a^3$.

where the sums extend over all N fluid particles inside the simulation box. Here, the change in the momentum, $\Delta \mathbf{p}_i(t)$, of a particle i in a collision step is given by

$$\Delta \mathbf{p}_i(t) = m(\mathbf{v}_i(t) - \hat{\mathbf{v}}_i(t)), \quad (22)$$

where $\hat{\mathbf{v}}_i$ is the particle velocity after streaming and before collision. The superscripts u and l indicate that the considered quantity is calculated at the upper and lower wall, respectively. Note that Eqs. (20) and (21) account also for momentum exchange due to collisions with phantom particles located inside wall boundary cells (bc). The negative sign in front of the transversal momentum ex-

change Δp_{ix}^l accounts for the negative velocity, $-u$, of the lower wall. In Eq. (21), the second term on the right-hand side describes the momentum change at time t_q due to particle collisions with the wall at time t_q^w . In the considered setup, only particles of fluid phase B collide with the walls, hence $\Delta t_q^i = h_B - (t_q - t_q^w)$. On performing a time average, which for the ergodic system equals an ensemble average, the equality $\langle \sigma_{xz}^e \rangle = \langle \sigma_{xz}^i \rangle$ is expected to hold, where $\langle \dots \rangle$ denotes the time (ensemble) average. The time interval Δt over which time averages are performed is very small in comparison with the viscous diffusion time across a layer thickness, i.e. $\Delta t = h_A = 0.02 t_0$ for A -fluid and $\Delta t = h_B = 0.1 t_0$ for B -fluid properties. Note that for the internal stress calculation which invokes also the momentum exchange of fluid A and B particles described by the third term on the rhs of Eq. (21)), the time average is performed separately for each phase, owing to the different collision times h_A and h_B . Note further that Eq. (20) consists of an upper wall part, $\sigma_{xz}^{e,u}$, and a lower wall part, $\sigma_{xz}^{e,l}$, each in accord with the force-per-area definition of the wall stress.

MPC results for the average external and internal shear stresses, in units of the thermal stress $\sigma_0 = k_B T/a^3$, are presented in Fig. 3(b), as functions of time t after the two walls started to move at $t = 0^+$, with instantaneous velocities $\pm u$ in the initially quiescent fluid system. The external upper (dashed blue line) and lower (dashed red line) stress values are shown separately, and are compared with the average internal stress curve (green). The two wall stresses coincide at all times, and decay monotonically from the maximal value at $t = 0^+$ toward the plateau value of $0.08 \times \sigma_0$ where the steady-state regime is reached, the latter characterized by the fully developed piece-wise linear shear profile in Fig. 3(a). The interior stress increases accordingly from its value zero at $t = 0^+$, where the bulk fluid is still at rest, toward its steady-state value which, as expected, agrees with the steady-state value of the exterior stress. The characteristic transition time for the external shear stress relaxation (and internal stress buildup) toward the uniform steady-state value is given by $\tau_v = (L/4)^2 (1/\nu_A + 1/\nu_B) \approx 140 \times t_0$, which is the viscous diffusion time across half of the simulation cell length. From the limiting stress value and steady-state flow profiles, the viscosity values $\eta_A/\eta_0 = 42.9$ and $\eta_B/\eta_0 = 9.1$ are deduced, which agree within less than 5% error with the viscosity values obtained from analytical theory for respective one-component MPC fluids (cf. Sec. IID).

The shear viscosities of the binary fluid model can be easily controlled by a single parameter, namely the collision time step h , but there is a continuous viscosity crossover along the MPC interface of thickness comparable to the collision cell. In general, the continuum hydrodynamic behavior is accurately recovered by the MPC simulations for lengths larger than about $2a$ [14].

IV. HYDRODYNAMIC CORRELATIONS: TRANSVERSE VELOCITY AUTO-CORRELATION FUNCTION

Additional insight into the time-resolved hydrodynamic behavior of the MPC fluid is gained by analyzing the transverse velocity auto-correlation function (TVCF) [14] in the various layers. For a stationary and isotropic Newtonian fluid in a volume V with periodic boundary conditions, the linearized Landau-Lifshitz Navier-Stokes equations yields the single-exponentially decaying TVCF in Fourier space [14]

$$\langle \mathbf{u}^T(\mathbf{k}, t)^T \cdot \mathbf{u}^T(-\mathbf{k}, 0) \rangle = \frac{2k_B T}{\rho V} e^{-\nu k^2 t}. \quad (23)$$

Here, $\mathbf{u}^T(\mathbf{k}, t)$ is the Fourier-transformed velocity part perpendicular to the wave vector \mathbf{k} [14, 86], i.e., $\mathbf{u}^T \cdot \mathbf{k} = 0$. The brackets denote an equilibrium ensemble average, with the fluid system at rest on hydrodynamic time and length scales. The factor 2 on the rhs accounts for the two independent transversal modes. Owing to isotropy, the TVCF depends only on the modulus $k = |\mathbf{k}|$ of the wave vector. Simulation results for the TVCF of a single-phase MPC fluid are in excellent agreement with the above hydrodynamic prediction [14, 86, 87].

To explore thermally induced transverse velocity correlations in our three-layer model of fluids A and B , we perform simulations for a cubic simulation box of size $L = 80a$, with periodic boundary conditions in all three Cartesian coordinate directions. The higher-viscosity layer A of width $L/2$ is symmetrically sandwiched between two fluid- B layers, as illustrated in Fig. 2, but now for a system without shear. The periodic boundary condition along the z -axis implies an alternating pattern of horizontal A and B layers of equal thickness $L/2$.

We determine the TVCFs of the pure A and B fluids in the three-layer model by considering N_o MPC particles inside an observation cuboid of z -thickness $L_o = L/4 = 20a$ and volume $V_o = L \times L \times L_o$, symmetrically located inside the A -fluid and B -fluid layers, respectively. To explore additionally the influence of the fluid interface, the TVCF for another observation cuboid with smaller vertical width $L_o = 10a$ is determined, with the cuboid symmetrically enclosing the A - B interface. The Fourier transform, $\mathbf{u}(\mathbf{k}, t)$, of the fluid velocity fluctuations in an observation cuboid is calculated according to

$$\mathbf{u}(\mathbf{k}, t) = \frac{1}{N_o} \sum_{i=1}^{N_o} \mathbf{v}_i(t) e^{i\mathbf{k} \cdot \mathbf{r}_i(t)}, \quad (24)$$

where $\mathbf{v}_i(t)$ is the velocity of fluid particle i at position $\mathbf{r}_i(t)$ inside the considered cuboid. For the cuboid centered around the A - B interface, half of the particles summed over are, on average, of A -type and half of B -type. For the present purpose, we consider only wave vectors $\mathbf{k} = \mathbf{k}_{\parallel}$ parallel to the xy -plane, with wavelength $\lambda = 2\pi/k$ smaller than the cuboid width L_o . This re-

duces boundary artifacts due to fluid particles leaving or entering the observation cuboid.

Figure 4(a) displays the normalized TVCFs

$$C_v^T(\mathbf{k}, t) = \frac{\langle \mathbf{u}^T(\mathbf{k}, t) \cdot \mathbf{u}^T(-\mathbf{k}, 0) \rangle}{\langle \mathbf{u}^T(\mathbf{k}, 0) \cdot \mathbf{u}^T(-\mathbf{k}, 0) \rangle} \quad (25)$$

of the fluid inside the A and B cuboids, respectively, as well as the TVCF of the mixed-fluid cuboid enclosing the A - B interface. The horizontally oriented wavenectors employed here are $\mathbf{k} = (32\pi/L)(1, 0, 0)$ and $\mathbf{k} = (32\pi/L)(0, 1, 0)$, of wavelength $\lambda = 5a$ smaller than the cuboid width. Notice that $\mathbf{u}^T(\mathbf{k}, t) = (\mathbf{1} - \mathbf{k} \otimes \mathbf{k}/k^2)\mathbf{u}(\mathbf{k}, t)$. Owing to the non-isotropic three-layer structure, $C_v^T(\mathbf{k}, t)$ is in principle an anisotropic function of the wave vector, depending also on the vertical location and width of the considered cuboid.

Within the correlation time window $t \leq 3t_0$ depicted in Figure 4(a), the MPC-calculated normalized TVCFs of the pure A and B -fluid cuboids (open symbols) decay exponentially according to $\exp(-k^2\nu t)$, with kinematic viscosity values ν_A and ν_B as numerically obtained in Sec. III. The reason why the isotropic bulk fluid TVCF form is recovered in the anisotropic three-layer system (within numerical accuracy) is that the viscous diffusion time, $\tau_\nu^{A,B} = (L/8)^2/\nu_{A,B}$, over a distance from the cuboid center to the interface is large compared to the resolved correlation time window; the viscous diffusion times are $\tau_\nu^A = 24t_0$ and $\tau_\nu^B = 115t_0$, respectively. Hence, in the considered time window and the considered wave vector of wavelength $\lambda = 5a$, the velocity correlations in the single-fluid cuboids are yet unperturbed by the interfaces.

On the same basis one could expect that the MPC data for the TVCF of the cuboid symmetrically enclosing the A - B interface (green circles in Figure 4(a)) are for $t \leq 3t_0$ decently well reproduced by the superposition of two bulk-fluid exponential TVCFs according to

$$C_v^{T,int}(\mathbf{k}, t) = \xi_A e^{-\nu_A k^2 t} + \xi_B e^{-\nu_B k^2 t}, \quad (26)$$

for equal weight factors $\xi_A = \xi_B = 1/2$, and ν_A and ν_B determined from the MPC simulation data for the single-fluid layers. The equal-weight superposition according to Eq. (26) is represented by the dashed dark-green line. For $t > t_0$, this line somewhat underestimates the MPC-TVCF data, reflecting the growing influence of the interfacial region with increasing time. A fit of the simulation data by Eq. (26), for unchanged values of ν_A and ν_B , yields the weight factors $\xi_A = 0.541$ and $\xi_B = 1 - \xi_A = 0.469$ (dark-green solid line). The asymmetry could be a consequence of the shorter viscous diffusion time across the half-width $L_0/2$ for the fluid- A part of the two-fluid observation cuboid.

The time integral of the normalized TVCF (25), characterizing a one-component fluid in the hydrodynamic regime, is

$$T(\mathbf{k}, t) = \int_0^t dt' C_v^T(\mathbf{k}, t') = \frac{1}{\nu_\alpha k^2} \left(1 - e^{-\nu_\alpha k^2 t} \right), \quad (27)$$

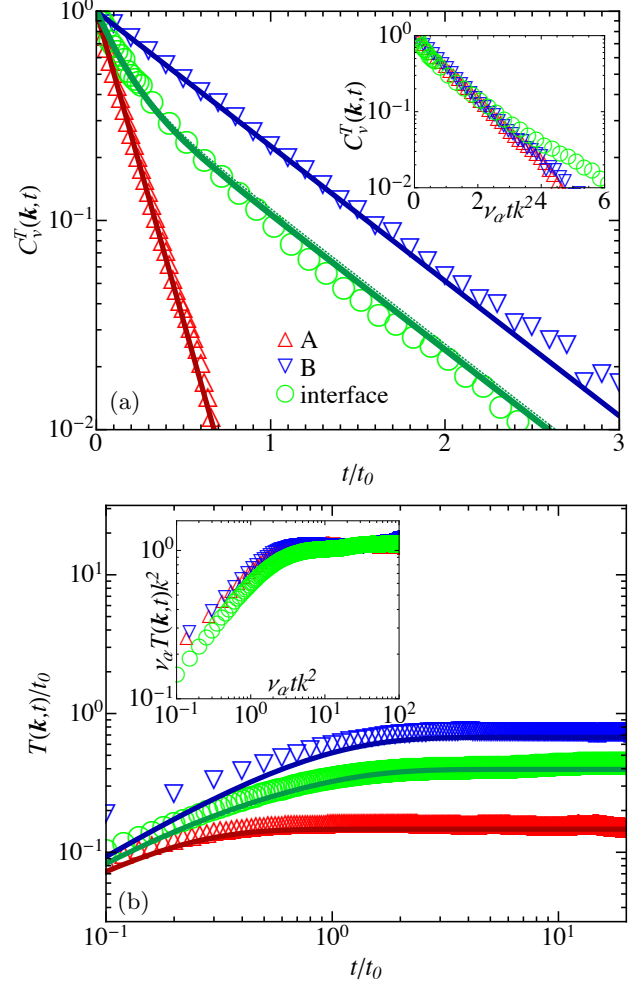


FIG. 4: (a) Normalized TVCFs, $C_v^T(\mathbf{k}, t)$, for a wave vector \mathbf{k} parallel to xy -plane with wavelength $\lambda = 5a$ obtained from MPC simulations for the fluid A (red, up triangles), B (blue, down triangles), and the A - B interface cuboid (green, circles). The corresponding solid lines represent the bulk-fluid prediction $\exp(-\nu_{A,B} k^2 t)$ and the double-exponential expression in Eq. (26) with weights $\xi_A = 0.541 = 1 - \xi_B$ (green solid line) and $\xi_A = \xi_B = 1/2$ (green dotted line), respectively. Inset: TVCF dependence on $\nu_\alpha k^2 t$ for $\alpha \in \{A, B, \text{int}\}$ and $\nu_{\text{int}} = \nu_A \nu_B / [\xi_A \nu_A + \xi_B \nu_B]$. (b) Time-integrated normalized TVCFs, $T(\mathbf{k}, t)$ (27). Solid lines represent Eq. (27) and (28), respectively. Inset: data collapse for $\nu_\alpha k^2 t$.

where $T(\mathbf{k}, t)$, in the limit $t \rightarrow \infty$, is related to the Oseen tensor in reciprocal space [14, 85, 88]. The accordingly time-integrated TVCF in Eq. (26) for the cuboid enclosing the interfacial region is

$$T^{\text{int}}(\mathbf{k}, t) = \frac{\xi_A}{\nu_A k^2} \left(1 - e^{-\nu_A k^2 t} \right) + \frac{\xi_B}{\nu_B k^2} \left(1 - e^{-\nu_B k^2 t} \right), \quad (28)$$

with $T^{\text{int}}(\mathbf{k}, \infty) = 1/k^2 \nu_{\text{int}}$ and $\nu_{\text{int}} = \nu_A \nu_B / [\xi_A \nu_A +$

$\xi_B \nu_B]$.

The time dependence of $T(\mathbf{k}, t)$ and $T^{int}(\mathbf{k}, t)$ for the three observation cuboids, obtained from the data of Fig. 4(a), are shown in Fig 4(b). The time-integrated MPC simulation data (open symbols) agree overall well with the analytic expressions in Eqs. (27) and (28) based on the single-fluid theoretical expressions. As shown in the inset, the time-integrated TVCFs are universal functions of $\nu_\alpha k^2 t$, as expected by the identical universal behavior of the TVCFs. The factor $\nu_{int} = \nu_A \nu_B / [\xi_A \nu_B + \xi_B \nu_A]$ can be considered as a common effective kinematic viscosity of the A and B fluid contributions in the cuboid enclosing the interface. The inset further illustrates that the crossover to the long-time plateau values $1/(k^2 \nu_\alpha)$ is characterized by the viscous diffusion times $\tau_k^\alpha = (\nu_\alpha k^2)^{-1} = 0.63a^2/\nu_\alpha$. Since $\tau_k^A < \tau_k^{int} < \tau_k^B$, the Stokesian regime of inertia-free, quasi-instantaneous hydrodynamics is reached for the considered wavenumber at times distinctly smaller than the viscous diffusion time across the colloid diameter $(2R)^2/\nu_B = 29t_0 \gg \tau_k^B$.

V. MOBILITY OF A COLLOIDAL SPHERE NEAR A FLUID-FLUID INTERFACE

The (strong) viscosity difference between two immiscible fluid phases affects the dynamics of a colloidal particle moving near the fluid interface. To explore the hydrodynamic coupling, and to scrutinize the according MPC coupling predictions in our three-layer model, we calculate the mobility coefficients of a sphere embedded in fluid A which moves steadily under low-Reynolds-number conditions parallel or perpendicular to the planar A - B interfaces. The coefficients are determined as functions of the reduced distance $d_z = z/(2R)$ of the sphere center from the A - B interface (see Fig. 5). To reduce finite-size effects due to the periodic boundary conditions in z -direction, different from Secs. IV, we consider a non-cubic simulation box of lengths $2L_x = 2L_y = L_z = 80a$, i.e., a box twice as large in the z -direction than the other spatial directions.

As indicated in Fig. 5, the sphere of radius $R = 2.5a$ is subjected to a weak constant force F_{\parallel} (F_{\perp}) applied to its center, and oriented parallel (perpendicular) to the fluid-fluid interface. Due to the no-slip boundary conditions employed on the sphere surface, the moving sphere drags nearby fluid along, which is compensated by fluid backflow such that the total momentum of the system in any spatial direction is zero (quiescent fluid system assumed) [29, 90]. Under low-Reynolds-conditions, where in the continuum mechanics picture the fluid flow is described by the quasi-stationary linear Stokes equation, the reduced translational mobilities follow from the relations

$$\Gamma_{\parallel}(d_z) = 6\pi\eta_A R \frac{\langle v_{\parallel} \rangle(d_z)}{F_{\parallel}}, \quad (29)$$

$$\Gamma_{\perp}(d_z) = 6\pi\eta_A R \frac{\langle v_{\perp} \rangle(d_z)}{F_{\perp}} \quad (30)$$

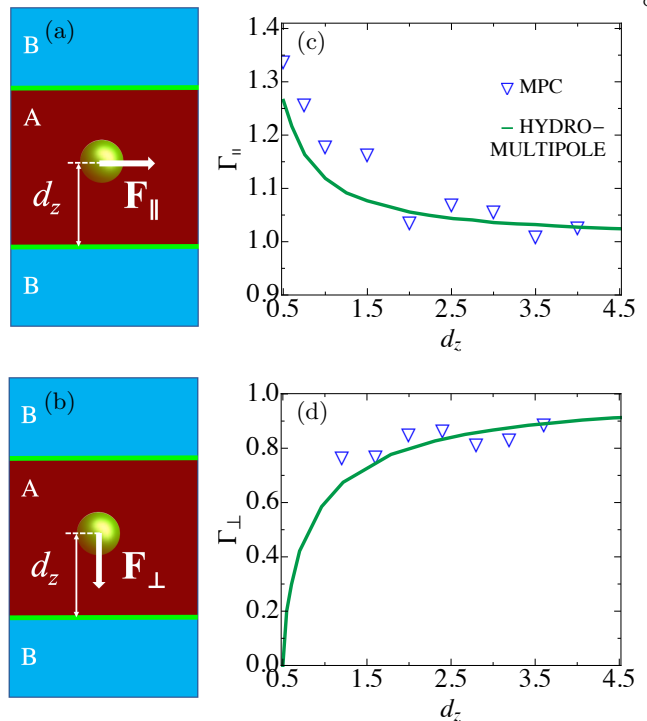


FIG. 5: (a) and (b) Schematics of the three-layer system for determining the lateral and transverse translational mobility coefficients, Γ_{\parallel} and Γ_{\perp} , of a no-slip sphere of radius $R = 2.5a$ embedded in fluid A , as functions of the reduced distance $d_z = z/(2R)$ from the sphere center to the A - B interface. The employed viscosity ratio is $\eta_B/\eta_A = 0.21$. (c) and (d) Lateral and transverse mobility coefficients from MPC simulations (symbols) and hydrodynamic force-multipole-expansion calculations (green lines) [89] in units of the bulk mobility value $1/(6\pi\eta_A R)$.

by measuring the steady-state mean velocity $\langle v_{\parallel,\perp} \rangle$ of the sphere for a given constant force $F_{\parallel,\perp}$. In our MPC simulations, the thermal force value $F_{\parallel,\perp} = 4k_B T/a$ is used. After applying the force to the sphere, the steady-state with constant mean drift velocity is reached for times $t \gg R^2/\nu_A$. Note that $\Gamma_{\parallel,\perp} = 1$ in the bulk region of fluid, distant from any interface or boundary [85].

Figures 5(c) and (d) display the MPC results (open blue symbols) for the normalized lateral and transverse mobilities, $\Gamma_{\parallel}(d_z)$ and $\Gamma_{\perp}(d_z)$, as functions of the reduced distance $d_z = z/(2R)$. For comparison, according reduced mobilities are shown (green solid lines) as obtained numerically using an elaborate Stokesian dynamics-based hydrodynamic force-multipole expansion method, encoded in the software package HYDROMULTIPOLE [89]. The depicted mobility curves by the force multipoles method, valid under creeping-flow conditions, are taken from [89] and constitute accurate continuum hydrodynamics results for a no-slip sphere in a half-infinite Newtonian fluid A which moves steadily parallel or perpendicular to an ideally flat and clean interface of zero interfacial viscosity and Marangoni stress. The interface separates the fluid- A half-space from the fluid- B half-

space. Note that $\Gamma_{\parallel,\perp}$ depend on the ratio of the shear viscosities of the two fluids.

Both the MPC simulation and continuum hydrodynamic results predict the lateral sphere mobility to increase with decreasing distance d_z from the A - B interface. They are in good overall agreement, except for small distances where the simulation data are somewhat larger (see Fig. 5 (c)). Regarding the transverse mobility depicted in Fig. 5 (d), the continuum hydrodynamics curve for Γ_{\perp} decreases strongly with decreasing distance, and assumes the value $\Gamma_{\perp} = 0$ at the sphere-interface contact distance $d_z = 0.5$ due to lubrication. In contrast, while the MPC simulation data in Fig. 5 (d) are in accord with a mild decline of the mobility for decreasing distance $d_z \gtrsim 1.5$, they do not reproduce the strong drop in Γ_{\perp} at small distances $d_z \lesssim 1$ (i.e., $z \lesssim 5a$). On first sight, this discrepancy is surprising, since friction and lubrication effects for a hard-sphere colloid embedded in a single MPC fluid close to a *solid* no-slip wall are well reproduced [91]. However, it can be attributed qualitatively to the mixing of the two fluids in the interfacial region over a thickness larger than a collision cell size a , and to a local perturbation of the hydrodynamic flow field by the no-slip sphere moving normally to the nearby interface. In the HYDROMULTIPOLE calculations, the two fluid half-spaces are taken as ideally incompressible, and the interface as ideally thin and flat, without any sphere-induced perturbation. Notice further that the sphere size is comparable with the MPC interfacial thickness. At any rate, the MPC implementation of immiscible fluids captures the dynamics of the immersed colloidal sphere overall quite well.

VI. SUMMARY AND CONCLUSIONS

In this article, we have developed a MPC-based mesoscale hydrodynamic simulation scheme for modeling immiscible (layered) binary fluids with viscosity contrast separated by a flat interface.

Shear flow, shear stress, fluctuating hydrodynamic velocity correlations, and hydrodynamic mobilities of an embedded spherical particle moving close to a flat fluid interface have been analyzed using a three-layered MPC fluid, and validated against continuum hydrodynamics predictions. From the shear flow simulations, we obtained a piece-wise linear flow profile in excellent agreement with the continuum hydrodynamics prediction. By computing the shear stress in relation to the shear rate, we confirmed that the analytically obtained viscosity values for single-phase MPC fluids are reproduced by the binary fluid model, in regions distant from the fluid-fluid interface. This agreement is due to the good accuracy of MPC viscosity calculations already on the level of a collision cell, and the fact that the thickness of the interface is small compared to the transverse spatial extension of the single-fluid A and B layers in the periodic simulation box.

To examine the predictions by our two-fluids MPC model regarding time-dependent correlations of thermally induced velocity fluctuations, we calculated the transverse velocity auto-correlation function (TVCF) in different observation cuboids. We showed that the TVCFs for the single-fluid cuboids follow closely the expected exponential decay, characterized by the kinematic viscosity of the respective fluid and the considered wave number. In contrast, the calculated TVCF of the cuboid enclosing the A - B interface is overall well fitted by a linear combination of the exponential TVCFs for bulk fluids A and B , using the viscosity values determined in our shear-flow studies. The approximate validity of linear superposition suggests that the TVCF of the cuboid is only mildly affected by the interfacial region. A stronger interfacial influence can be expected for a narrower cuboid of width smaller than the employed value $L_o = 10a$.

Finally, we have probed the hydrodynamic coupling of a steadily moving no-slip sphere to a nearby flat two-fluids interface by determining its hydrodynamic mobilities. The distance dependence of the lateral mobility coefficient for the three-layers MPC model agrees well with the according mobility result by a hydrodynamic force-multipole expansion method for a sphere moving close to an ideally flat, clean interface separating two incompressible fluids. While decent agreement is observed also regarding the transverse mobility for sphere-interface distances larger than three times the sphere radius, the sharp mobility decline at small distances predicted by the continuum hydrodynamics approach for a non-deformable planar interface of zero thickness, is not obtained by the MPC simulations. We attribute this to the mixing of the two fluids in the MPC interfacial region of thickness larger than the collision cell size a , and the local perturbation of the interface caused by the transverse motion of the sphere. Moreover, and different from what is assumed in the force multipoles calculation, the two fluids in the MPC model are compressible. The non-zero compressibility of the fluids plays a role in particular for transverse (i.e., squeezing) sphere motions. To reduce the influence of the finite interface width on the sphere mobilities, a significantly larger sphere can be considered. Moreover, an alternative method to determine the mobilities may be better suited [91] in order to reduce fluid perturbations by the translating sphere.

A numerical advantage of the two-fluids MPC model is that the desired viscosities of the fluid phases can be easily prescribed using the analytic viscosity expression for a single-phase MPC fluid [14]. Compared to other mesoscale simulation models of immiscible binary fluids, the present model is straightforwardly implemented, since it does not involve the computation of thermodynamic properties and kinetic processes related to phase separation. Hence, the computational cost is comparable to simulating two single-phase MPC fluids with different collision times.

The two-fluids MPC simulation method can be applied to a wide range of biological soft matter systems. For ex-

ample, the approach can be suitably extended to study interfacial rheological properties including interfacial viscosity [92, 93] and interfacial tension. Furthermore, as noted already in the introduction, the model can be applied to investigate the lateral self- and collective diffusion of different in-membrane or membrane-attached proteins. The effects of the viscosity contrast between a membrane and the adjacent cytosol, and hydrodynamic interactions between proteins and membrane, and among the proteins, on protein diffusion can be simulated over several timescales using a simplifying coarse-graining of the system. In a more refined analysis, lipid molecules and other macromolecules forming the membrane constitute a crowded environment which slows down the diffusion of embedded proteins [94]. Molecular crowding effects cause so-called sub-diffusion, identified recently to play a vital role in many biological phenomena [95–98], including neuronal signaling [99, 100]. For future assessment, molecular crowding mechanism can be implemented into our three-layer model, with the middle layer playing the role of the membrane, by adding a planar layer of interacting host particles to the middle layer, or alternatively and more realistically, by account-

ing for visco-elastic effects in the middle layer through semi-atomistic memory function calculations. Work by us in both directions is in progress.

Furthermore, the present MPC model can be extended to interfaces with imposed sinusoidal fluctuations mimicking membrane fluctuations. Moreover, the quantitative control of viscosity values opens the possibility to study systems with designed viscosity gradients. This provides a means to study the dynamics of biological macromolecules or microorganisms responding to viscosity gradients, such as in viscotaxis [101].

ACKNOWLEDGMENTS

The authors gratefully acknowledge computing time granted through JARA-HPC on the supercomputer JU-RECA at Forschungszentrum Jülich [102]. ZT thanks Marisol Ripoll for valuable discussions. This work is embedded in the joint IBI-INM project on mesoscale modeling of intracellular signaling events underlying neuron functions.

-
- [1] D. H. Rothman and J. M. Keller, *J. Stat. Phys.* **52**, 1119 (1988).
 - [2] A. K. Gunstensen, D. H. Rothman, S. Zaleski, and G. Zanetti, *Phys. Rev. A* **43**, 4320 (1991).
 - [3] Y. Yu, H. Liu, D. Liang, and Y. Zhang, *Phys. Fluids* **31**, 012108 (2019).
 - [4] X. Shan and H. Chen, *Phys. Rev. E* **47**, 1815 (1993).
 - [5] X. Shan and H. Chen, *Phys. Rev. E* **49**, 2941 (1994).
 - [6] E. Orlandini, M. R. Swift, and J. M. Yeomans, *EPL* **32**, 463 (1995).
 - [7] M. R. Swift, E. Orlandini, W. R. Osborn, and J. M. Yeomans, *Phys. Rev. E* **54**, 5041 (1996).
 - [8] X. He, X. Shan, and G. D. Doolen, *Phys. Rev. E* **57**, R13 (1998).
 - [9] J. Lombard, I. Pagonabarraga, and E. Corvera Poiré, *Phys. Rev. Fluids* **5**, 064201 (2020).
 - [10] P. V. Coveney and P. Español, *J. Phys. A Math. Theor.* **30**, 779 (1997).
 - [11] A. Malevanets and R. Kapral, *J. Chem. Phys.* **110**, 8605 (1999).
 - [12] G. Gompper, T. Ihle, D. Kroll, and R. Winkler, *Adv. Polym. Sci.*, **221**, 1 (2009).
 - [13] R. Kapral, *Adv. Polym. Sci.*, **140**, 89 (2008).
 - [14] C.-C. Huang, G. Gompper, and R. G. Winkler, *Phys. Rev. E* **86**, 056711 (2012).
 - [15] C.-C. Huang, G. Gompper, and R. G. Winkler, *J. Chem. Phys.* **138**, 144902 (2013).
 - [16] M. Yang, M. Theers, J. Hu, G. Gompper, R. G. Winkler, and M. Ripoll, *Phys. Rev. E* **92**, 013301 (2015).
 - [17] M. Theers, E. Westphal, G. Gompper, and R. G. Winkler, *Phys. Rev. E* **93**, 032604 (2016).
 - [18] M. Liebetreu, M. Ripoll, and C. N. Likos, *ACS Macro Lett.* **7**, 447 (2018).
 - [19] A. Martin-Gomez, T. Eisenstecken, G. Gompper, and R. G. Winkler, *Phys. Rev. E* **101**, 052612 (2020).
 - [20] N. Kikuchi, A. Gent, and J.M. Yeomans, *Eur. Phys. J. E* **9**, 63 (2002).
 - [21] K. Mussawisade, M. Ripoll, R. G. Winkler, and G. Gompper, *J. Chem. Phys.* **123**, 144905 (2005),.
 - [22] R. Chelakkot, R. G. Winkler, and G. Gompper, *Phys. Rev. Lett.* **109**, 178101 (2012).
 - [23] J. F. Ryder and J. M. Yeomans, *J. Chem. Phys.* **125**, 194906 (2006).
 - [24] S. Frank and R. G. Winkler, *EPL* **83**, 38004 (2008).
 - [25] C.-C. Huang, R. G. Winkler, G. Sutmann, and G. Gompper, *Macromolecules* **43**, 10107 (2010).
 - [26] M. Ripoll, R. G. Winkler, and G. Gompper, *Phys. Rev. Lett.* **96**, 188302 (2006).
 - [27] S. P. Singh, D. A. Fedosov, A. Chatterji, R. G. Winkler, and G. Gompper, *J. Phys. Condens. Matter* **24**, 464103 (2012).
 - [28] S. P. Singh, R. G. Winkler, and G. Gompper, *Phys. Rev. Lett.* **107**, 158301 (2011).
 - [29] J. T. Padding and A. A. Louis, *Phys. Rev. Lett.* **93**, 220601 (2004).
 - [30] M. Ripoll, P. Holmqvist, R. G. Winkler, G. Gompper, J. K. G. Dhont, and M. P. Lettinga, *Phys. Rev. Lett.* **101**, 168302 (2008).
 - [31] Z. Tan, M. Yang, and M. Ripoll, *Soft Matter* , 7283 (2017).
 - [32] S. Bucciarelli, J. S. Myung, B. Farago, S. Das, G. A. Vliegthart, O. Holderer, R. G. Winkler, P. Schurtenberger, G. Gompper, and A. Stradner, *Sci. Adv.* **2**, e1601432 (2016).
 - [33] S. Das, J. Riest, R. G. Winkler, G. Gompper, J. K. Dhont, and G. Nägele, *Soft Matter* **14**, 92 (2018).

- [34] H. Noguchi and G. Gompper, *Phys. Rev. Lett.* **93**, 258102 (2004).
- [35] H. Noguchi and G. Gompper, *Proc. Natl. Acad. Sci. U. S. A.* **102**, 14159 (2005).
- [36] J. Hu, M. Yang, G. Gompper, and R. G. Winkler, *Soft Matter* **11**, 7867 (2015).
- [37] M. Wagner and M. Ripoll, *EPL* **119**, 66007 (2017).
- [38] K. Qi, E. Westphal, G. Gompper, and R. G. Winkler, *Phys. Rev. Lett.* **124**, 068001 (2020).
- [39] Y.-G. Tao and R. Kapral, *Soft Matter* **6**, 756 (2010).
- [40] A. Zöttl and H. Stark, *Phys. Rev. Lett.* **108**, 218104 (2012).
- [41] S. B. Babu and H. Stark, *New J. Phys.* **14**, 085012 (2012).
- [42] J. Elgeti and G. Gompper, *Proc. Natl. Acad. Sci. U. S. A.* **110**, 4470 (2013).
- [43] S. Y. Reigh, R. G. Winkler, and G. Gompper, *Soft Matter* **8**, 4363 (2012).
- [44] M. Theers and R. G. Winkler, *Soft Matter* **10**, 5894 (2014).
- [45] M. Yang and M. Ripoll, *Soft Matter* **10**, 1006 (2014).
- [46] S. M. Mousavi, G. Gompper, and R. G. Winkler, *Soft Matter* **16**, 4866 (2020).
- [47] M. Yang and M. Ripoll, *Soft Matter* **12**, 8564 (2016).
- [48] Z. Tan, M. Yang, and M. Ripoll, *Phys. Rev. Applied* **11**, 054004 (2019).
- [49] Y. Hashimoto, Y. Chen, and H. Ohashi, *Comput. Phys. Commun.* **129**, 56 (2000).
- [50] Y. Inoue, Y. Chen, and H. Ohashi, *J. Comput. Phys.* **201**, 191 (2004).
- [51] T. Ihle, E. Tüzel, and D. M. Kroll, *EPL* **73**, 664 (2006).
- [52] E. Tüzel, G. Pan, T. Ihle, and D. M. Kroll, *EPL* **80**, 40010 (2007).
- [53] E. Tüzel, G. Pan, and D. M. Kroll, *J. Chem. Phys.* **132**, 174701 (2010),.
- [54] C. Echeverria, K. Tucci, O. Alvarez-Llamoza, E. Orozco-Guillén, M. Morales, and M. Cosenza, *Front. Phys.* **12**, 1 (2017).
- [55] T. Hiller, M. Sanchez de La Lama, and M. Brinkmann, *J. Comput. Phys.* **315**, 554 (2016).
- [56] T. Eisenstecken, R. Hornung, R. G. Winkler, and G. Gompper, *EPL* **121**, 24003 (2018).
- [57] R. Pesché, M. Kollmann, and G. Nägele, *J. Chem. Phys.* **114**, 8701 (2001).
- [58] G. Nägele, A. J. Banchio, M. Kollmann, and R. Pesché, *Mol. Phys.* **100**, 2921 (2002).
- [59] S. Panzuela, R. P. Peláez, and R. Delgado-Buscalioni, *Phys. Rev. E* **95**, 012602 (2017).
- [60] S. Panzuela and R. Delgado-Buscalioni, *Phys. Rev. Lett.* **121**, 048101 (2018).
- [61] B. U. Felderhof, *J. Chem. Phys.* **123**, 184903 (2005).
- [62] K. Huang and I. Szlufarska, *Nat. Commun.* **6**, 1 (2015).
- [63] D. Lopez and E. Lauga, *Phys. Fluids* **26**, 071902 (2014).
- [64] J. Hu, A. Wysocki, R. G. Winkler, and G. Gompper, *Sci. Rep.* **5**, 9586 (2015).
- [65] P. Janmey and P. Kinnunen, *Trends in Cell Biology* **16**, 538 (2006).
- [66] R. Kapoor, T. A. Peyear, R. E. Koeppe, and O. S. Andersen, *J. Gen. Physiol.* **151**, 342 (2019).
- [67] J. Corrie, L. Dey, J. D. Therien, and J. E. Baenziger, *Nat. Chem. Biol.* **9**, 701 (2013).
- [68] L. O. Romero, A. E. Massey, A. D. Mata-Daboin, F. J. Sierra-Valdez, S. C. Chauhan, J. F. Cordero-Morales, and V. Vásquez, *Nat. Commun.* **10**, 1 (2019).
- [69] R. Caires, F. J. Sierra-Valdez, J. R. Millet, J. D. Herwig, E. Roan, V. Vásquez, and J. F. Cordero-Morales, *Cell Rep.* **21**, 246 (2017).
- [70] J. Oates and A. Watts, *Curr. Opin. Struct. Biol.* **21**, 802 (2011).
- [71] M. Manna, M. Niemelä, J. Tynkkynen, M. Javanainen, W. Kulig, D. J. Müller, T. Rog, and I. Vattulainen, *Elife* **5**, e18432 (2016).
- [72] A. Malevanets and R. Kapral, *J. Chem. Phys.* **112**, 7260 (2000).
- [73] T. Ihle and D. M. Kroll, *Phys. Rev. E* **63**, 020201 (2001).
- [74] T. Ihle and D. M. Kroll, *Phys. Rev. E* **67**, 066706 (2003).
- [75] C.-C. Huang, A. Varghese, G. Gompper, and R. G. Winkler, *Phys. Rev. E* **91**, 013310 (2015).
- [76] R. G. Winkler and C.-C. Huang, *J. Chem. Phys.* **130**, 074907 (2009).
- [77] J. Padding, A. Wysocki, H. Löwen, and A. Louis, *J. Phys. Condens. Matter* **17**, S3393 (2005).
- [78] A. Zöttl and H. Stark, *Phys. Rev. Lett.* **112**, 118101 (2014).
- [79] M. Theers, E. Westphal, G. Gompper, and R. G. Winkler, *Soft Matter* **12**, 7372 (2016).
- [80] M. Theers, E. Westphal, K. Qi, R. G. Winkler, and G. Gompper, *Soft Matter* **14**, 8590 (2018).
- [81] A. Lamura, G. Gompper, T. Ihle, and D. M. Kroll, *EPL* **56**, 319 (2001).
- [82] M. Hecht, J. Harting, T. Ihle, and H. J. Herrmann, *Phys. Rev. E* **72**, 011408 (2005).
- [83] T. Ihle, E. Tüzel, and D. M. Kroll, *Phys. Rev. E* **72**, 046707 (2005).
- [84] H. Noguchi, N. Kikuchi, and G. Gompper, *EPL* **78**, 10005 (2007).
- [85] J. Dhont, *An Introduction to Dynamics of Colloids*, Elsevier Science, (1996).
- [86] M. Theers and R. G. Winkler, *Phys. Rev. E* **91**, 033309 (2015).
- [87] E. Tüzel, T. Ihle, and D. M. Kroll, *Phys. Rev. E* **74**, 056702 (2006).
- [88] M. Doi and S. Edwards, *The Theory of Polymer Dynamics*, Clarendon Press, (1988).
- [89] J. Bławdziewicz, M. L. Ekiel-Jeżewska, and E. Wajnryb, *J. Chem. Phys.* **133**, 114702 (2010).
- [90] S. P. Singh, G. Gompper, and R. G. Winkler, *J. Chem. Phys.* **148**, 084901 (2018).
- [91] J. T. Padding and W. J. Briels, *J. Chem. Phys.* **132**, 054511 (2010).
- [92] S. Shkulipa, W. den Otter, and W. Briels, *Biophys. J.* **89**, 823 (2005).
- [93] W. den Otter and S. Shkulipa, *Biophys. J.* **93**, 423 (2007).
- [94] D. M. Engelman, *Nature* **438**, 578 (2005).
- [95] A. P. Minton, *Curr. Opin. Struct. Biol.* **10**, 34 (2000).
- [96] J. S. Kim and A. Yethiraj, *Biophys. J.* **96**, 1333 (2009).
- [97] Y. Wang, M. Sankar, A. E. Smith, A. S. Krois, and G. J. Pielak, *J. Am. Chem. Soc.* **134**, 16614 (2012),.
- [98] H. Matsuda, G. Putzel, V. Backman, and I. Szleifer, *Biophys. J.* **106**, 1801 (2014).
- [99] M. Hellmann, D. W. Heermann, and M. Weiss, *EPL* **97**, 58004 (2012).
- [100] L. E. Sereshki, M. A. Lomholt, and R. Metzler, *EPL* **97**, 20008 (2012).
- [101] B. Liebchen, P. Monderkamp, B. ten Hagen, and H. Löwen, *Phys. Rev. Lett.* **120**, 208002 (2018).
- [102] Jülich Supercomputing Centre, *JLSRF* **4**, (2018) .